Supplementary Information:

Less atmospheric radiative heating due to aspherical dust with coarser size

Akinori Ito[1]*, Adeyemi A. Adebiyi[2], Yue Huang[2], and Jasper F. Kok[2]

[1]Yokohama Institute for Earth Sciences, JAMSTEC, Yokohama, Kanagawa, 236-0001, Japan. [2] Department of Atmospheric and Oceanic Sciences, University of California, Los Angeles, CA 90095, USA. *e-mail: akinorii@jamstec.go.jp

This document contains Supplementary Tables and Figures, which are summarized below:

- **Table S1.** Regionally averages of dust aerosol optical depth at 550 nm ($DAOD_{550}$) in summer (June, July, and August).
- **Table S2.** Regionally averages of dust aerosol optical depth at 550 nm ($DAOD_{550}$) in winter (December, January, and February), spring (March, April, and May), and autumn (September, October, and November).
- **Table S3.** Comparison of model estimates with semi-observation-based data of dust clear-sky SW radiative effect efficiency at the surface ($W \cdot m^{-2}$ $DAOD^{-1}$).
- **Table S4.** Comparison of model estimates with semi-observation-based data of dust clear-sky SW radiative effect efficiency at TOA ($W \cdot m^{-2}$ $DAOD^{-1}$).
- **Table S5.** Comparison of model estimates with semi-observation-based data of dust clear-sky LW radiative effect efficiency at the surface ($W \cdot m^{-2}$ $DAOD^{-1}$).
- **Table S6.** Comparison of model estimates with semi-observation-based data of dust clear-sky LW radiative effect efficiency at TOA ($W \cdot m^{-2}$ $DAOD^{-1}$).
- **Figure S1.** Comparison of semi-observation-based and modeled $DAOD_{550}$ in summer. Results were shown for default (blue square), improved (red circles), and fine-global (black triangles) simulations. The dashed line represented a 1 : 1 correspondence. The summer season was shown because most semi-observation-based data on dust radiative effects were available. The comparison for other seasons was presented in Table S2.
- **Figure S2.** Comparison of semi-observation-based and modeled dust SW radiative effect efficiency in summer. Results were shown at the surface (red circles) and TOA (blue square) from (a) default, (b) improved, (c) fine-global, (d) coarse-region, (e) coarse-mineral, (f) coarse-absorption simulations. The dashed line represented a 1 : 1 correspondence. The correlation coefficients (r) and root mean square errors (RMSE) were also shown. The regionally averaged values were listed in Tables S3 and S4 at the surface and TOA, respectively.
- **Figure S3.** Summertime dust SW radiative effect efficiency. The model results were shown (a) and (b) fine-global, (c) and (d) coarse-region, (e) and (f) coarse-mineral, and (g) and (h) coarse-mineral coarse-absorption simulations at the surface and TOA, respectively. The regionally averaged values were listed in Tables S3 and S4 at the surface and TOA, respectively.
- **Figure S4.** Comparison of semi-observation-based and modeled dust LW radiative effect efficiency in summer. Results were shown at the surface (red circles) and TOA (blue square) from (a) default, (b) improved, (c) fine-global, (d) coarse-global, (e) coarse-region, (f) coarse-absorption. The dashed line represented a 1 : 1 correspondence. The correlation coefficients (r) and root mean square errors (RMSE) were also shown. The regionally averaged values were listed in Tables S5 and S6 at the surface and TOA, respectively.
- **Figure S5.** Summertime dust LW radiative effect efficiency. The model results were shown (a) and (b) fine-global, (c) and (d) coarse-global, (e) and (f) coarse-region, and (g) and (h) coarse-absorption simulations at the surface and TOA, respectively. The regionally averaged values were listed in Tables S5 and S6 at the surface and TOA, respectively.

Table S1. Regionally averages of dust aerosol optical depth at 550 nm ($DAOD_{550}$) in summer (June, July, and August).

Region name	Region coordinates	Semi-observation-based data	Default simulation	Improved simulation	Fine-global simulation
Mid-Atlantic	4°–40°N, 50°–20°W	0.143 ± 0.005	0.094	0.083	**0.148**
African West Coast	10°–34°N, 20°–5°W	0.365 ± 0.016	**0.357**	0.294	0.563
Northern Africa	26°–40°N, 5°W–30°E	0.207 ± 0.016	**0.197**	**0.194**	0.310
Mali/Niger	10°–26°N, 5°W–10°E	0.462 ± 0.044	**0.379**	**0.397**	0.597
Bodele/Sudan	10°–26°N, 10°–40°E	0.310 ± 0.018	**0.297**	0.349	0.469
Northern Middle East	26°–40°N, 30°–50°E	0.164 ± 0.015	0.209	**0.168**	0.327
Southern Middle East	0°–26°N, 40°–67.5°E	0.330 ± 0.044	0.438	0.384	0.691
Kyzyl Kum	26°–50°N, 50°–67.5°E	0.154 ± 0.034	0.307	**0.201**	0.481
Thar	20°–50°N, 67.5°–75°E	0.319 ± 0.029	0.167	0.156	**0.265**
Taklamakan	30°–50°N, 75°–92.5°E	0.171 ± 0.026	0.040	0.094	0.064
Gobi	36°–50°N, 92.5°–115°E	0.102 ± 0.035	**0.032**	**0.117**	**0.051**
North America	20°–45°N, 80°–130°W	0.028 ± 0.010	**0.010**	**0.030**	**0.016**
South America	0°–55°S, 80°–55°W	0.010 ± 0.006	**0.009**	**0.013**	**0.015**
Southern Africa	10°–35°S, 10°–40°E	0.013 ± 0.005	**0.014**	**0.020**	**0.022**
Australia	10°–40°S, 110°–160°E	0.010 ± 0.005	**0.005**	**0.013**	**0.008**
Correlation coefficients			0.86	0.91	0.86
Root mean square errors			0.08	0.06	0.16

Semi-observation-based data of the $DAOD_{550}$ were averaged over 2004–2008 (Ridley et al., 2016; Adebiyi et al., 2020). The bold represents the data which fell within ± 2 times standard deviation of the measurements. The correlation coefficients and root mean square errors were also shown. The scatter plot was shown in Fig. S1.

Table S2. Regionally averages of dust aerosol optical depth at 550 nm ($DAOD_{550}$) in winter (December, January, and February), spring (March, April, and May), and autumn (September, October, and November).

	Winter			Spring			Autumn		
Region name	Semi-observation-based	Default	Improved	Semi-observation-based	Default	Improved	Semi-observation-based	Default	Improved
Mid-Atlantic	0.064 ± 0.013	**0.045**	**0.072**	0.106 ± 0.008	0.026	0.034	0.084 ± 0.006	0.024	0.027
African West Coast	0.180 ± 0.010	0.129	0.223	0.250 ± 0.019	0.127	0.145	0.233 ± 0.022	0.132	0.149
Northern Africa	0.118 ± 0.011	0.029	**0.108**	0.219 ± 0.010	0.174	**0.200**	0.151 ± 0.016	0.092	**0.134**
Mali/Niger	0.257 ± 0.019	0.215	0.377	0.441 ± 0.022	0.341	0.358	0.277 ± 0.023	0.247	**0.268**
Bodele/Sudan	0.191 ± 0.006	0.149	0.360	0.339 ± 0.023	**0.34**	0.406	0.212 ± 0.021	0.223	0.276
Northern Middle East	0.112 ± 0.011	0.038	0.165	0.223 ± 0.011	0.169	**0.226**	0.113 ± 0.019	0.115	**0.133**
Southern Middle East	0.123 ± 0.018	0.056	**0.144**	0.204 ± 0.021	0.096	**0.176**	0.150 ± 0.020	0.157	**0.135**
Kyzyl Kum	0.115 ± 0.017	0.028	**0.116**	0.176 ± 0.026	0.096	**0.204**	0.101 ± 0.018	0.129	0.138
Thar	0.130 ± 0.029	0.024	**0.094**	0.238 ± 0.033	0.091	**0.173**	0.135 ± 0.037	0.072	**0.072**
Taklamakan	0.119 ± 0.013	0.008	0.029	0.275 ± 0.027	**0.03**	0.110	0.104 ± 0.011	0.016	0.045
Gobi	0.093 ± 0.022	0.006	0.028	0.192 ± 0.022	0.053	**0.183**	0.047 ± 0.021	0.018	0.091
North America	0.010 ± 0.005	**0.003**	**0.027**	0.029 ± 0.011	**0.014**	**0.031**	0.012 ± 0.006	0.006	0.014
South America	0.019 ± 0.011	**0.024**	**0.016**	0.013 ± 0.007	**0.013**	**0.011**	0.016 ± 0.009	0.022	**0.013**
Southern Africa	0.016 ± 0.007	**0.02**	**0.011**	0.011 ± 0.005	**0.009**	**0.009**	0.016 ± 0.007	0.028	**0.012**
Australia	0.025 ± 0.013	**0.016**	**0.028**	0.013 ± 0.006	**0.008**	**0.012**	0.023 ± 0.011	0.020	**0.020**
Correlation coefficients		0.83	0.89		0.84	0.89		0.88	0.88
Root mean square errors		0.06	0.06		0.10	0.06		0.05	0.04

Semi-observation-based data of the $DAOD_{550}$ were averaged over 2004–2008 (Ridley et al., 2016; Adebiyi et al., 2020). The bold represents the data which fell within ± 2 times standard deviation of the measurements. The correlation coefficients and root mean square errors were also shown.

Table S3. Comparison of model estimates with semi-observation-based data of dust clear-sky SW radiative effect efficiency at the surface ($W \cdot m^{-2}$ $DAOD^{-1}$).

Number	Month	Semi-observation-based	Default	Improved	Fine-global	Coarse-global	Coarse-region	Coarse-mineral	Coarse-absorption
2	6,7,8	–65[a]	–63	–51	–43	–51	–49	–68	–39
3	6,7,8	–86[b]	–69	–56	–47	–56	–53	–74	–43
12	9	69[c]	–58	–45	–39	–45	–44	–60	–34
14	4,5,6	–60[d]	–56	–44	–41	–44	–42	–53	–33

Region number is defined in Table 4. The radiative effect efficiency is defined as the gradient of the linea least square fit applied to the $DAOD_{550}$ and dust radiative effect at each grid. The area weighted averages for land or ocean are listed. [a]Li et al. (2004). [b]Song et al. (2018). [d]Di Biagio et al. (2010). [e]Hansell et al. (2012).

Table S4. Comparison of model estimates with semi-observation-based data of dust clear-sky SW radiative effect efficiency at TOA ($W \cdot m^{-2}$ $DAOD^{-1}$).

Number	Month	Semi-observation-based	Default	Improved	Fine-global	Coarse-global	Coarse-region	Coarse-mineral	Coarse-absorption
1	6,7,8	Near 0[a]	17	13	3	13	14	28	–1
2	6,7,8	–35 ± 3[b]	–13	–12	–18	–12	–13	–0.3	–20
3	6,7,8	–27[c]	–16	–15	–21	–15	–16	–0.7	–24
4	6,7,8	–48 ± 4[d]	–20	–17	–21	–17	–17	–6.9	–23
12	9	–46[e]	–22	–16	–22	–16	–16	–9.0	–20

Region number is defined in Table 4. The radiative effect efficiency is defined as the gradient of the linea least square fit applied to the $DAOD_{550}$ and dust radiative effect at each grid. The area weighted averages for land or ocean are listed. [a]Yang et al. (2009). [b]Li et al. (2004). [c]Song et al. (2018). [d]Christopher and Jones (2007). [e]Di Biagio et al. (2010). [f]Hansell et al. (2012).

Table S5. Comparison of model estimates with semi-observation-based data of dust clear-sky LW radiative effect efficiency at the surface ($W \cdot m^{-2}$ $DAOD^{-1}$).

Number	Month	Semi-observation-based data	Default	Improved	Fine-global	Coarse-global	Coarse-region	Coarse-mineral	Coarse-absorption
3	6,7,8	24[a]	8.8	21	7.5	12	13	21	16
13	9	16[b]	16	30	13	18	19	30	24
14	4,5,6	31–35[c]	22	33	18	20	22	33	25

Region number is defined in Table 4. The radiative effect efficiency is defined as the gradient of the linea least square fit applied to the $DAOD_{550}$ and dust radiative effect at each grid. The area weighted averages for land or ocean are listed. [a]Song et al. (2018). [b]Hansell et al. (2010). [c]Hansell et al. (2012).

Table S6. Comparison of model estimates with semi-observation-based data of dust clear-sky LW radiative effect efficiency at TOA ($W \cdot m^{-2}$ $DAOD^{-1}$).

Number	Month	Semi-observation-based data	Default	Improved	Fine-global	Coarse-global	Coarse-region	Coarse-mineral	Coarse-absorption
1	6,7,8	24 ± 1.3[a]	8.3	19.9	7.2	11.0	10.8	19.9	14.5
3	6,7,8	9.5[b]	4.3	11.6	3.8	5.8	6.1	11.6	8.1
4	6,7,8	9.0 ± 3.5[c]	3.5	9.7	3.1	4.9	5.1	9.7	6.9
5	6,7,8	22[d]	6.8	16.1	5.8	8.8	8.6	16.1	11.6
5	9	15[e]	5.5	11.7	4.8	6.2	6.0	11.7	8.4
6	6,7,8	17[d]	7.6	20.3	6.6	11.1	11.6	20.3	14.5
6	9	20[e]	7.3	16.1	6.4	8.5	8.9	16.1	11.5
7	6,7,8	16[d]	9.1	21.0	7.9	11.9	11.9	21.0	15.6
7	9	21[e]	6.3	14.5	5.5	8.1	7.4	14.5	10.7
8	6,7,8	21[d]	5.7	13.5	5.0	7.3	6.8	13.5	9.8
8	9	19[e]	5.1	8.7	4.4	4.7	4.4	8.7	6.4
9	6,7,8	25[d]	5.1	11.7	4.5	5.9	5.5	11.7	8.2
9	9	1[e]	4.0	7.4	3.6	3.7	3.3	7.4	5.2
10	6,7,8	20[d]	6.6	14.1	5.8	7.2	6.9	14.1	9.9
10	9	11[e]	5.5	10.5	4.8	5.5	5.0	10.5	7.5
11	6,7,8	18[d]	8.4	19.0	7.4	9.9	9.1	19.0	13.5
11	9	11[e]	6.1	10.3	5.4	5.2	4.8	10.3	7.3
13	9	13[f]	4.4	30	3.8	18	19	30	24
14	4,5,6	17–21[g]	4.4	9.0	3.8	4.6	5.0	9.0	6.1

Region number is defined in Table 4. The radiative effect efficiency is defined as the gradient of the linea least square fit applied to the $DAOD_{550}$ and dust radiative effect at each grid. The area weighted averages for land or ocean are listed. [a]Yang et al. (2009). [b]Song et al. (2018). [c]Christopher and Jones (2007). [d]Brindley and Russell (2009). [e]Zhang and Christopher (2003). [f]Hansell et al. (2010). [g]Hansell et al. (2012).

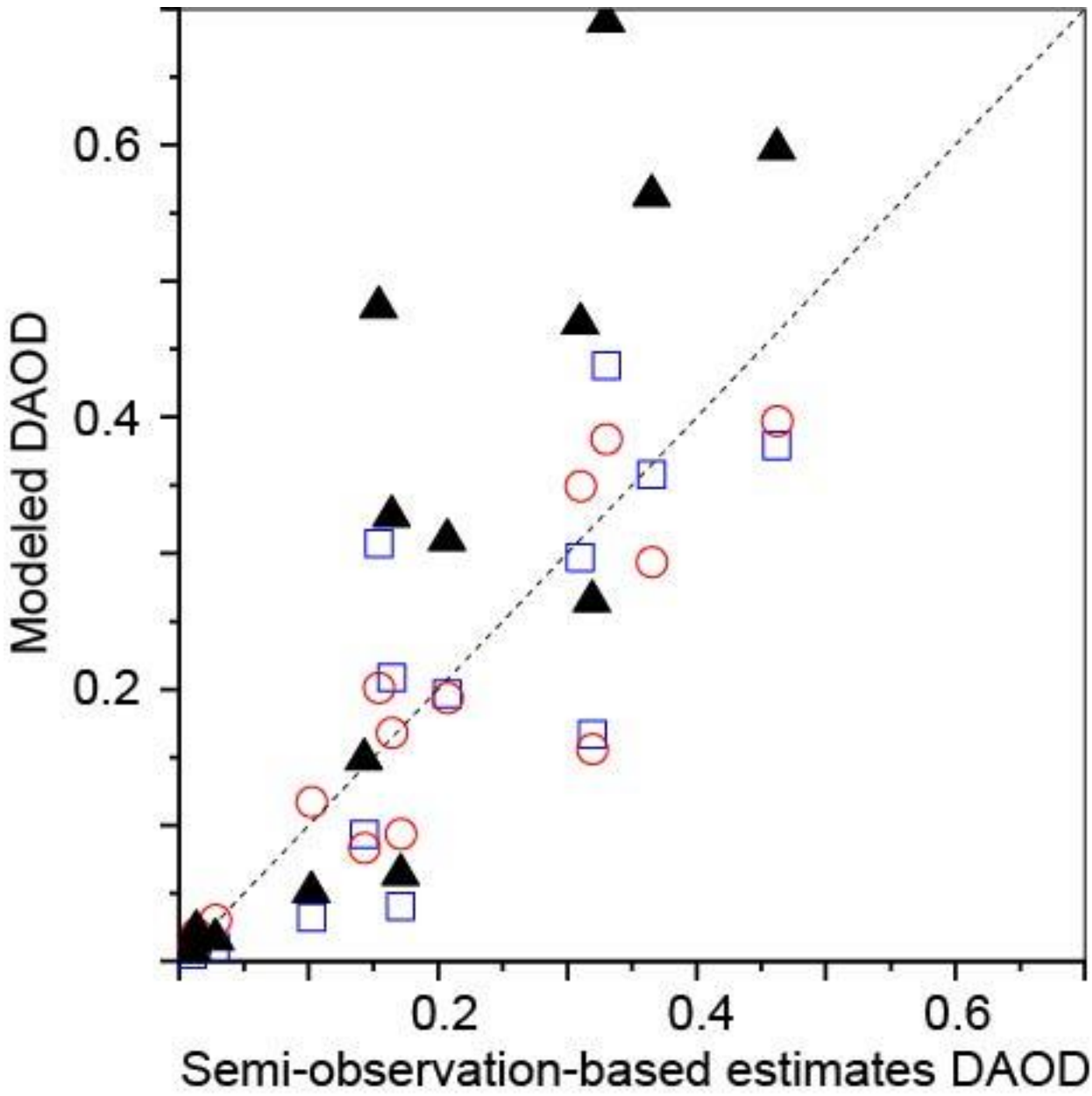

Figure S1. Comparison of semi-observation-based and modeled $DAOD_{550}$ in summer. Results were shown for default (blue square), improved (red circles), and fine-global (black triangles) simulations. The dashed line represented a 1 : 1 correspondence. The summer season was shown because most semi-observation-based data on dust radiative effects were available. The comparison for other seasons was presented in Table S2.

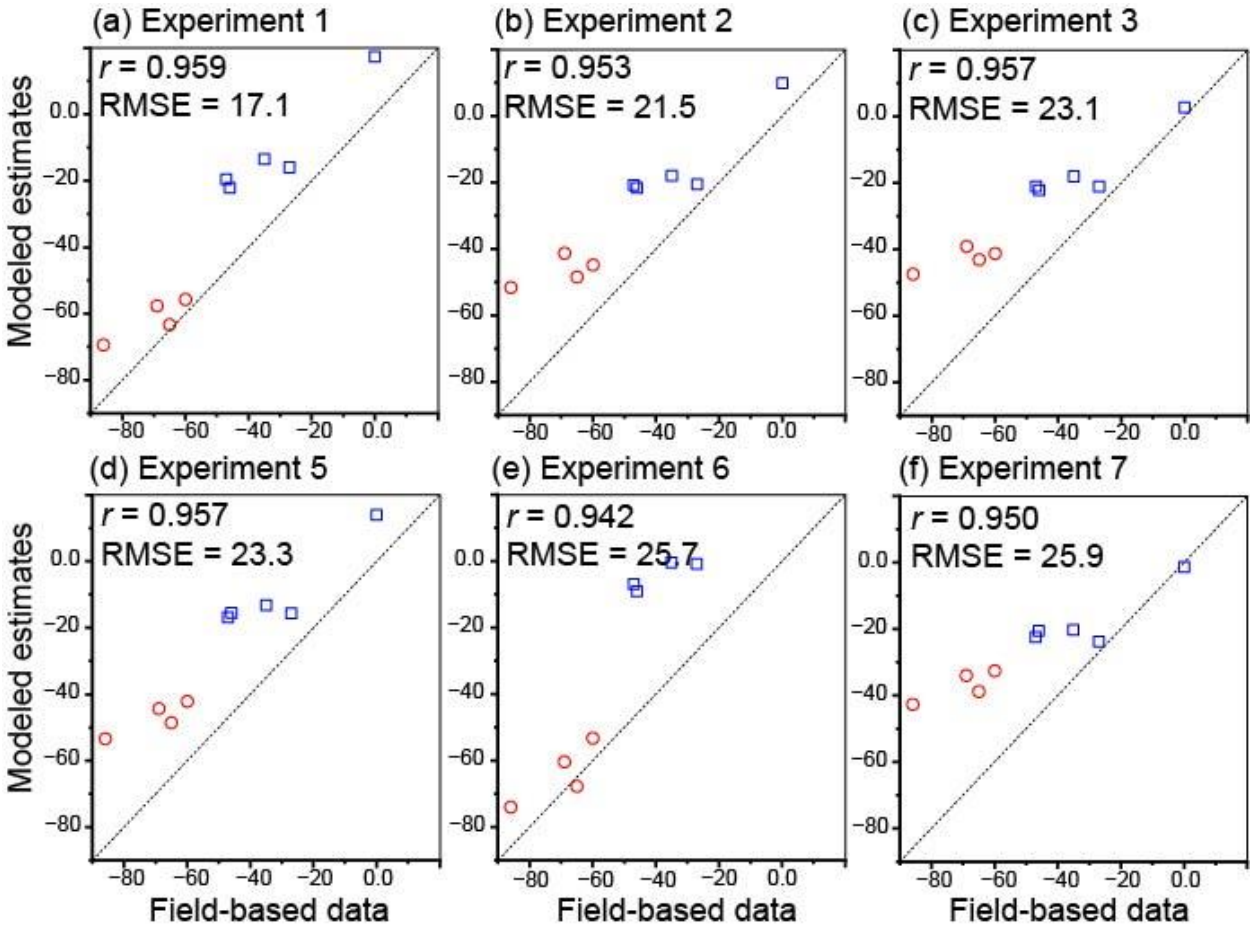

Figure S2. Comparison of semi-observation-based and modeled dust SW radiative effect efficiency in summer. Results were shown at the surface (red circles) and TOA (blue square) from (a) default, (b) improved, (c) fine-global, (d) coarse-region, (e) coarse-mineral, (f) coarse-absorption simulations. The dashed line represented a 1 : 1 correspondence. The correlation coefficients (*r*) and root mean square errors (RMSE) were also shown. The regionally averaged values were listed in Tables S3 and S4 at the surface and TOA, respectively.

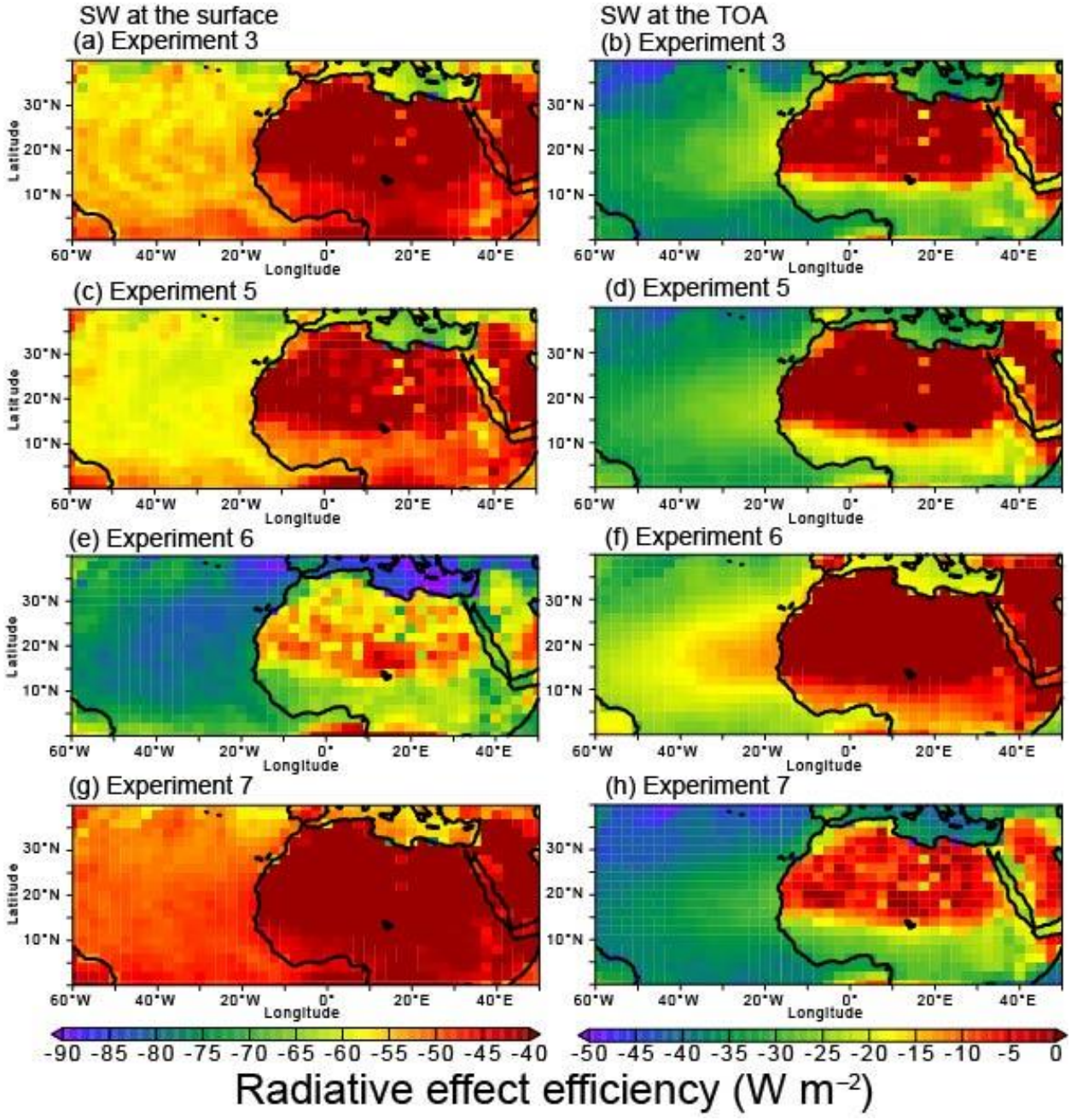

Figure S3. Summertime dust SW radiative effect efficiency. The model results were shown (a) and (b) fine-global, (c) and (d) coarse-region, (e) and (f) coarse-mineral, and (g) and (h) coarse-mineral coarse-absorption simulations at the surface and TOA, respectively. The regionally averaged values were listed in Tables S3 and S4 at the surface and TOA, respectively.

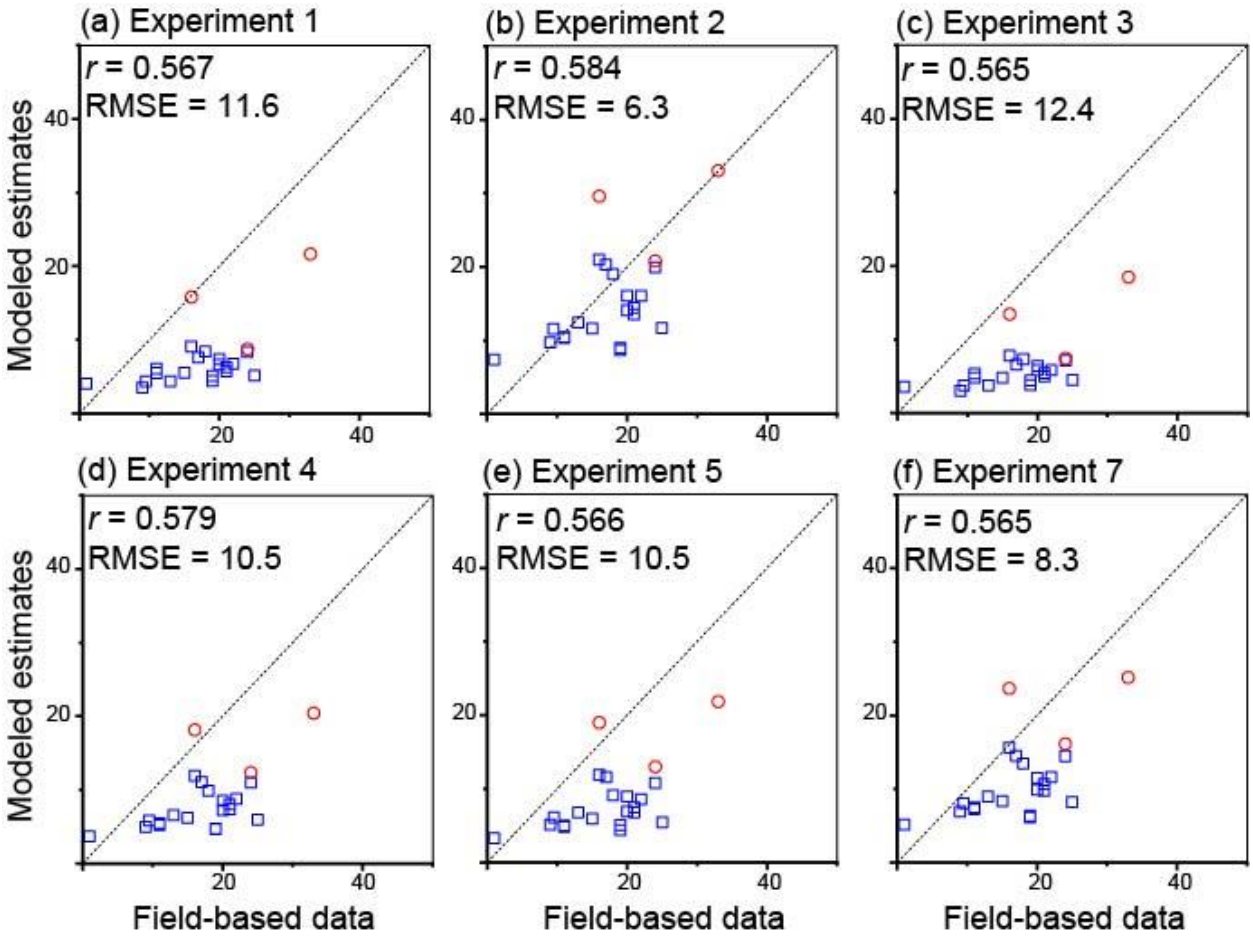

Figure S4. Comparison of semi-observation-based and modeled dust LW radiative effect efficiency in summer. Results were shown at the surface (red circles) and TOA (blue square) from (a) default, (b) improved, (c) fine-global, (d) coarse-global, (e) coarse-region, (f) coarse-absorption. The dashed line represented a 1 : 1 correspondence. The correlation coefficients (r) and root mean square errors (RMSE) were also shown. The regionally averaged values were listed in Tables S5 and S6 at the surface and TOA, respectively.

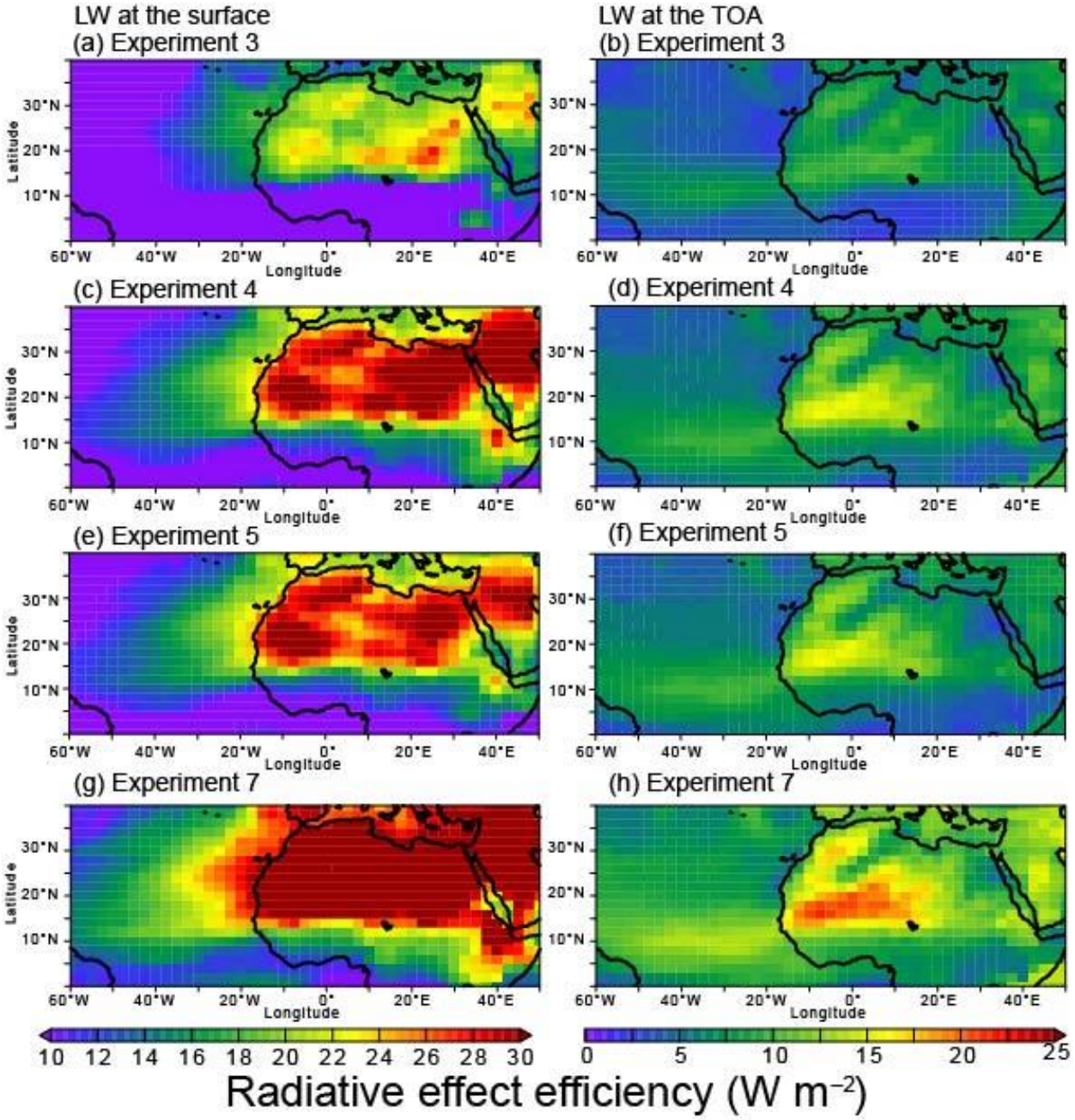

Figure S5. Summertime dust LW radiative effect efficiency. The model results were shown (a) and (b) fine-global, (c) and (d) coarse-global, (e) and (f) coarse-region, and (g) and (h) coarse-absorption simulations at the surface and TOA, respectively. The regionally averaged values were listed in Tables S5 and S6 at the surface and TOA, respectively.